Particle Accelerators
1983 Vol. 13 pp. 25–44
0031-2460/83/1301/0025$06.50/0

THE IMAGE-DISPLACEMENT EFFECT IN INTENSE ELECTRON BEAMS

R. J. ADLER, B. B. GODFREY, M. M. CAMPBELL, AND D. J. SULLIVAN

Mission Research Corporation, 1720 Randolph Road S.E., Albuquerque, New Mexico 87106 U.S.A.

and

T. C. GENONI†

Air Force Weapons Laboratory, Kirtland Air Force Base, New Mexico 87117 U.S.A.

(*Received October 21, 1982*)

A theoretical and experimental study of transverse beam motion in radial line accelerators due to image-displacement effects has been made. Both theory and experiment show that the thin-lens-gap approximation substantially overestimates the size of the displacement in the finite-length-gap parameter regime. An analytical treatment of the beam-gap coupling coefficient which allows a more accurate computation of the transverse impulse is described. A previously unrecognized drift motion in the gap is also discussed. Three-dimensional particle-in-cell numerical simulations of the experiment are presented for a wide range of magnetic guide field strengths. Finally, the possible impact of the image-displacement instability on RADLAC accelerators is determined.

I. INTRODUCTION

The radial pulseline linear induction accelerator is a promising new approach to producing high-current, high-energy, short-pulse electron beams.[1,2] It consists of a beam injector and several identical acceleration modules. The injector is a standard cold-cathode, pulsed-diode electron beam generator.[3] Leaving the injector, the beam is transported along a strong solenoidal magnetic guide field in an evacuated metal drift tube. The tube is interrupted at several axial locations by gaps across which additional accelerating voltages are applied. As the beam passes, the gaps are energized by radial transmission lines, which are in turn charged using pulsed-power technology. Very high beam energy can be achieved in principle simply by stringing together enough modules. No magnetic materials (e.g., ferrite) are used in the transmission lines. The resulting low transmission-line impedance dictates that the beam current be several tens of kiloamps. Space-charge constraints consequently require that the beam be annular and near the drift tube wall, unless the injector provides very high initial beam energy.

Illustrative of the radial pulseline accelerator concept is the RADLAC device, developed by Air Force Weapons Laboratory and Sandia National Laboratories.[4] Figure 1 is a schematic diagram. RADLAC accelerates a 25-kA, 15-nsec electron beam

† Present address: U.S. Military Academy, West Point, New York.

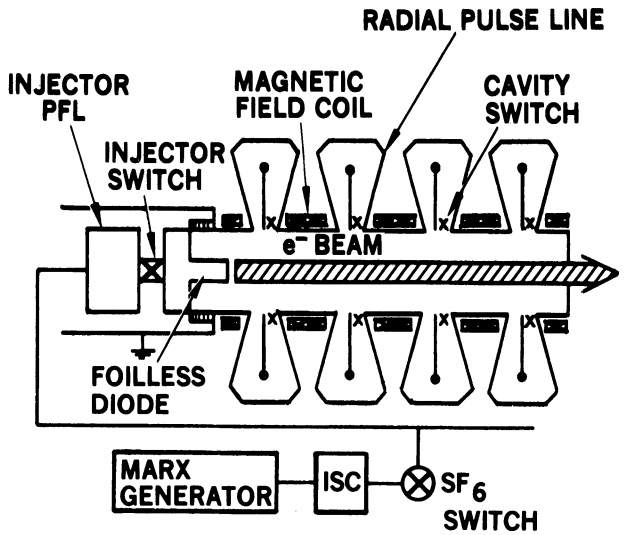

FIGURE 1 Schematic design of the RADLAC device, indicating the key accelerator components.

to 9 MeV using four nominally 2-MeV modules and a 2-MeV injector. The LIU-10 accelerator in the Soviet Union is larger, with fourteen modules and output parameters of 13.5 MeV, 50 kA and 20 to 40 nsec.[5]

Because the electron beam is the only system component linking the full accelerator voltage, stable beam transport replaces high-voltage breakdown as the key issue in demonstrating feasibility.[6] Field nonuniformity in the gaps can disturb the beam equilibrium, exciting a periodic, axisymmetric modulation of the beam envelope.[7,8] The gaps also can trigger beam breakup[9] and image-displacement instabilities.[10] Being annular, the electron beam is subject to diocotron instability and other azimuthal velocity shear phenomena, especially at low beam energy.[11–13] Finally, finite electrical conductivity of the metallic drift tube drives resistive-wall instabilities.[14] Preliminary analyses indicate that the RADLAC accelerator and modest enhancements to it are safe from these disruptive phenomena. More comprehensive investigations are in progress. This paper treats various aspects of the image-displacement effect.

The physical explanation of the image-displacement instability is straightforward. An uncentered beam in a uniform conducting pipe is attracted toward the nearest point on the wall by its electrostatic image concentrated there. Similarly, it is magnetostatically repelled by interaction with its $m = 1$ image current. The two forces cancel to order γ^{-2}, with the residual countered by the solenoidal guide field. At a gap, however, the image current is interrupted, while the image charge is but slightly displaced (for l/R not too large), giving rise to an abrupt transverse force on the beam in the direction of its initial lateral offset. The beam subsequently undergoes zero-frequency transverse oscillations as it travels to the next gap. Depending on the oscillation phase at the next gap, the oscillation will grow or not. The conceptual interaction of the beam with a single gap is illustrated in Fig. 2. It is also possible to analyze the image-displacement instability as the low-frequency limit of the beam-breakup mode,[15] although we shall not purse this route here.

Previous works by Woods[16] and Neil[17,18] were performed in the regime where the instability wavelength is much larger than the drift-tube radius, which in turn much exceeds the gap width. Typical radial-pulseline accelerator parameters are such that we

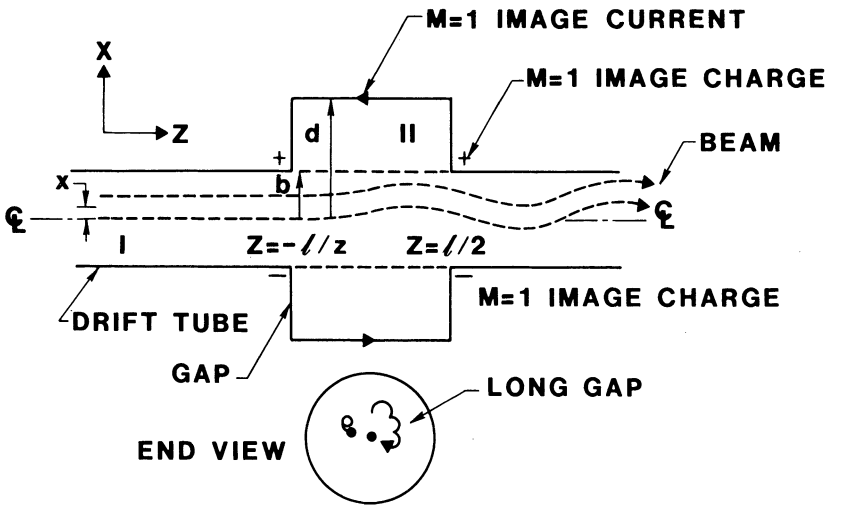

FIGURE 2 The offset image charge (+, −) and image current (arrows) in a gap in a drift tube. The beam is unperturbed on the left and oscillates on the right.

must relax this constraint. In Section II we first review the usual thin-gap expression and then generalize the results to gaps of finite width, analyzing the growth rate expression in several limits. A detailed evaluation of the $m = 1$ image fields at the gaps is presented in Section III. The experiments described in Section IV provide an upper bound on instability growth in strong applied magnetic fields. Good agreement with theory for both growth and precession rates is obtained. In Section V beam transverse-displacement amplification factors calculated from the finite-width-gap model of Section II and III are compared with experiments or three-dimensional simulations for a wide range of magnetic-field strengths. The rough agreement between model predictions and simulation output for weak guide fields suggests the need for additional research. Nonetheless, we are able to conclude in Section VI that radial pulseline accelerators of the RADLAC class are reasonably safe from severe image-displacement instabilities, based on numerical evaluation of instability growth during acceleration.

II. FINITE WIDTH GAP INTERACTION MODEL

In the region between gaps in a highly conducting drift tube, transverse oscillations of a disk of beam particles is described by

$$\frac{d}{dt}\gamma\frac{d}{dt}\xi = i\frac{d}{dt}\omega_c\xi + \frac{\omega_p^2 a\delta}{\gamma^2 b^2}\xi. \tag{1}$$

The first term on the right side of Eq. (1) is the restoring force of the applied axial magnetic field (with ω_c the corresponding cyclotron frequency), and the second is the net force between the beam and its $m = 1$ image in the drift tube wall. We take ξ as the complex sum of transverse displacements, $\xi = x + iy$. Other quantities are ω_p, the beam plasma frequency; γ, the particle relativistic energy; a, the mean radius

of the annular beam; δ, the thickness of the annulus; and b, the drift tube radius. The paraxial and low-frequency approximations are implicit in Eq. (1).

Typically, the second term in this equation is much smaller than the first for RADLAC parameters. The spatial variation of ξ between gaps is then approximately

$$\xi = \xi_1 + \xi_2 e^{ik_0 z}, \tag{2}$$

with ξ_1 and ξ_2 constants and $k_0 = \omega_c/\gamma$. (We choose units such that the speed of light is unity.) In other words, as the beam moves from one gap to the next the (complex) amplitude of the low-frequency space-charge mode is essentially constant, while the amplitude of the high-frequency cyclotron mode is multiplied by $\exp(i\omega_c L/\gamma)$, where L is the gap-to-gap separation.

In crossing a thin gap, the beam experiences an impulsive force $F\xi$, which changes its transverse velocity by $iF\xi/\omega_c$, but leaves the displacement constant. Combining this with Eq. (2) and taking γ to be constant for the moment, we find that the mode amplitudes evolve according to

$$\begin{pmatrix} \xi_2 \\ \xi_1 \end{pmatrix}^+ = e^{ik_0 L/2} \begin{pmatrix} \left(1 - \dfrac{iF}{k_0\gamma}\right) e^{ik_0 L/2} & -\dfrac{iF}{k_0\gamma} \\ \dfrac{iF}{k_0\gamma} & \left(1 + \dfrac{iF}{k_0\gamma}\right) e^{-ik_0 L/2} \end{pmatrix} \begin{pmatrix} \xi_2 \\ \xi_1 \end{pmatrix}^- \tag{3}$$

in passing through an accelerator module, consisting of a gap and drift-tube section, as in Fig. 2. The eigenvalues of Eq. (3) describe the growth of $m = 1$ gap-induced instabilities.

$$\begin{aligned} \lambda &= \psi \pm i\sqrt{1 - \psi^2} \\ \psi &= \cos k_0 L/2 + \frac{F}{k_0\gamma} \sin k_0 L/2 \end{aligned} \tag{4}$$

If $|\lambda| > 1$, growth occurs.

For the image-displacement instability,[16,18]

$$\frac{F}{k_0\gamma} \simeq \frac{l}{b^2} \frac{\omega_p{}^2 a\delta}{\omega_c}, \tag{5}$$

which is purely real. As a consequence, the requirement $|\lambda| < 1$ for stability reduces to $|\psi| \leq 1$. Figure 3 illustrates the dependence of ψ on $k_0 L/2$ for various values of $F/k_0\gamma$. Regions of stability and instability alternate as $k_0 L$ increases, although the stable bands shrink with larger F. The maximun value of ψ is

$$\psi_{\max} = [1 + (F/k_0\gamma)^2] \cos [\tan^{-1}(F/k_0\gamma)]. \tag{6}$$

It is evident from Fig. 3 that $F/k_0\gamma < 1/2$ is needed to assure minimal growth over several periodically spaced gaps with γ constant. If γ or L varies from gap to gap, the amplification after several gaps is determined by the eigenvalue of the matrix formed by multiplying the matrices from each gap as given in Eq. (3). In general, the eigenvalue of the product is much smaller than the product of the eigenvalues: Beam acceleration and irregular gap spacing cut image-displacement instability growth.

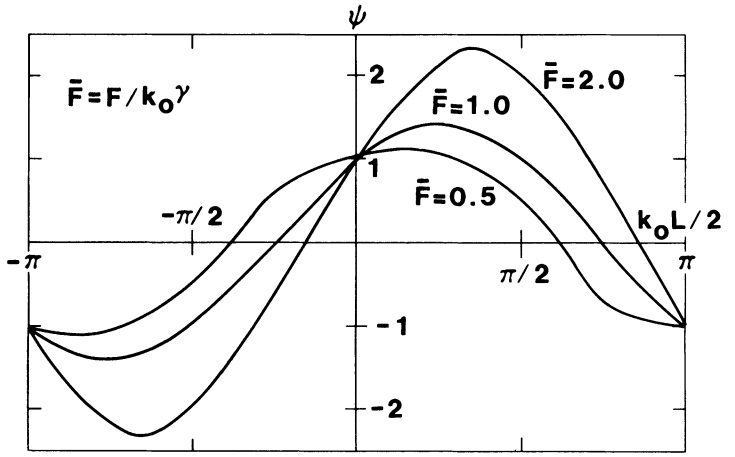

FIGURE 3 Image-displacement instability growth-parameter ψ from Eq. (4) as a function of the phase advance per gap.

Note that an alternative procedure for suppressing the image-displacement mode, choosing $k_0L/2$ to lie in a stability band, is impractical for radial pulseline accelerators. The wavenumber k_0 varies from shot to shot and even within shots; $k_0L/2$ is large.

As noted in the Introduction, the thin-gap approximation is not always well satisfied in radial pulseline accelerators. We can take account of finite gap width to lowest order by applying the gap force uniformly across the gap rather than as a delta-function at the gap center. Additionally, we replace the gap width l appearing in Eq. (5) with an effective width l_{eff} determined numerically by the procedure of Section III. Within the gap, the beam then supports normal modes of wavelength

$$\begin{aligned} k &= (k_0 \pm \alpha)/2, \\ \alpha^2 &= k_0{}^2 - 4F/\gamma l. \end{aligned} \tag{7}$$

The gap modes are matched in the usual manner to the drift-tube modes of Eq. (2) to derive an amplification matrix analogous to that of Eq. (3);

$$\begin{pmatrix} e^{ik_0(L-l)/2}\left[\cos(\alpha l/2) - i\dfrac{\sin(\alpha l/2)}{\alpha l/2}\left(\dfrac{F}{k_0\gamma} - \dfrac{k_0 l}{2}\right)\right] & -i\dfrac{F}{k_0\gamma}\dfrac{\sin(\alpha l/2)}{\alpha l/2} \\ i\dfrac{F}{k_0\gamma}\dfrac{\sin(\alpha l/2)}{\alpha l/2} & e^{ik_0(L-l)/2}\left[\cos(\alpha l/2) + i\dfrac{\sin(\alpha l/2)}{\alpha l/2}\left(\dfrac{F}{k_0\gamma} - \dfrac{k_0 l}{2}\right)\right] \end{pmatrix} \tag{8}$$

The eigenvalues of Eq. (8) are given by Eq. (4) with ψ redefined as

$$\psi = \cos\left(\frac{k_0(L-l)}{2}\right)\cos\left(\frac{\alpha l}{2}\right) + \left(\frac{F}{k_0\gamma} - \frac{k_0 l}{2}\right)\sin\left(\frac{k_0(L-l)}{2}\right)\sin\left(\frac{\alpha l}{2}\right)\Big/\left(\frac{\alpha l}{2}\right). \tag{9}$$

Let us compare instability behavior as predicted by the thin and thick gap models. For $\alpha^2 > 0$, the primary difference between Eqs. (4) and (9) is reduction in the latter

of the effective force per gap; i.e.,

$$\frac{F}{k_0\gamma} \to \left(\frac{F}{k_0\gamma} - \frac{k_0 l}{2}\right)\frac{\sin(\alpha l/2)}{\alpha l/2}. \tag{10}$$

To the extent that $F/k_0\gamma$ is less than $k_0 l/2$, finite gap width weakens the image-displacement instability. Note that ψ reduces the $\cos(k_0 L/2)$ irrespective of the magnitude of $k_0 l/2$ in the limit of vanishing F. For $\alpha^2 < 0$, on the other hand, exponential growth of the beam transverse displacement can occur in a single gap, as is evident from Eq. (7). This occurs for $F/k_0\gamma$ greater than $k_0 l/4$. Figure 4 plots k/k_0 versus $F/k_0{}^2\gamma l$. The exponential growth is, of course, unimportant for $\alpha l/2$ small. Indeed, for small gap widths, Eq. (9) reduces to Eq. (4) irrespective of the sign of α^2.

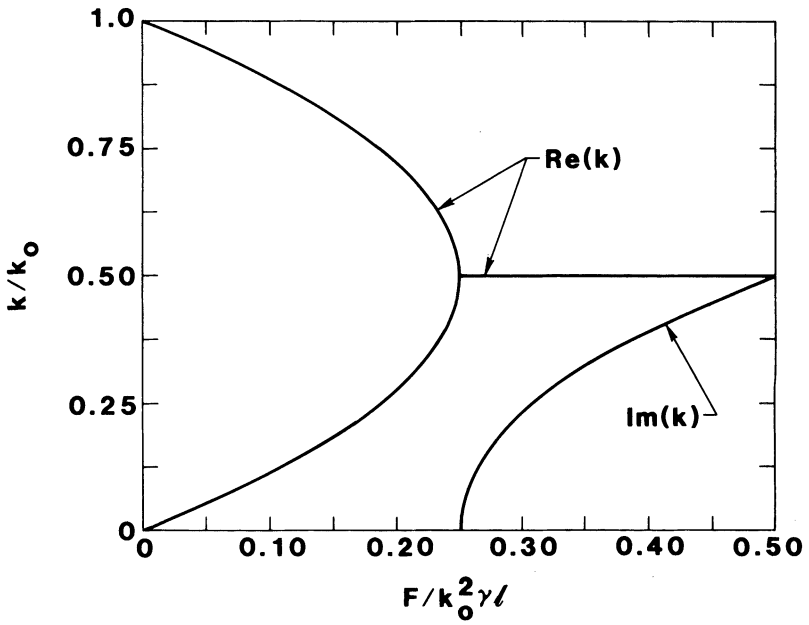

FIGURE 4 Spatial frequency and growth rate of beam oscillations in a single gap.

Growth per gap as determined by the two models is contrasted in Fig. 5 for parameters taken from Sections IV and V of this paper. [F is evaluated using $l_{\text{eff}} \simeq l$ in both sets of curves to focus attention on the explicit differences between Eqs. (4) and (9) only.] Sharp resonances occur in both cases for $2\pi/k_0 L - 1/n$, with n a positive integer. However, growth is much reduced when finite gap width is considered. $F/k_0\gamma - k_0 l/2$ is negative to the left of the small arrow at $2\pi/k_0 L = 1.31$. To the right of the other arrow, at 0.92, $\alpha^2 < 0$. For α^2 only slightly negative, no linear growth occurs (asymptotically) due to cancellations from gap to gap; the phase advance $k_0(L - \ell)$ is of order π. Substantial growth is predicted for α^2 strongly negative, beginning at $2\pi/k_0 L \simeq 1.4$.

Next we compute l_{eff}.

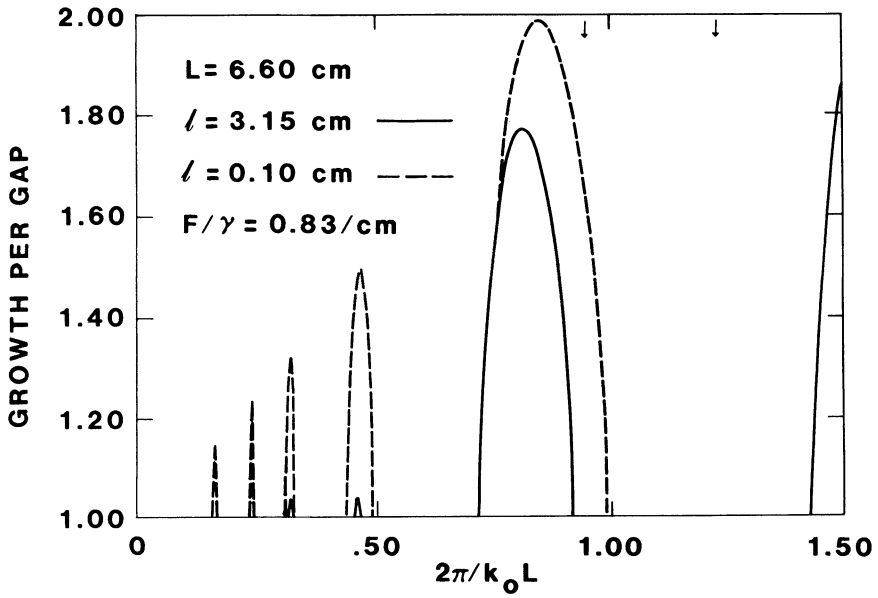

FIGURE 5 Comparison of instability growth for thick gap (solid curves) and thin gap (dashed curves) models.

III. IMAGE FORCES OF FINITE-WIDTH GAPS

As mentioned earlier, Eq. (5) is an accurate expression for the transverse force exerted on an off-center beam by a gap in the drift tube wall only for $l/b \ll 1$, the thin-lens limit. Provided $k_0 l$ is not too large, an improved expression based on the superposition principle can be obtained. The particle beam in a straight drift tube induces an $m = 1$ image charge on the tube wall of magnitude

$$\sigma/\xi = \omega_p{}^2 a\delta/b^2. \tag{11}$$

(The electron charge to mass ratio is taken as unity, and a factor of 4π is absorbed into σ.) The change in electric field due to a gap can therefore be associated with a canceling image charge $-\sigma$ in the gap opening at $r = b$.

Defining the gap electric field in terms of a potential V, we seek a solution to $\nabla^2 V = 0$ in the interiors of the drift tube and gap, with $V = 0$ on the conducting boundaries, $\partial V/\partial z = 0$ at $z \pm L/2$, and V satisfying appropriate matching conditions at $r = b, |z| < l/2$. Suppressing the azimuthal dependence, we write the potential in regions I and II as (regions I and II are delineated in Fig. 2),

$$V_I = A_0 \frac{r}{b} + \sum_n A_n I_1\left(\frac{2n\pi r}{L}\right)\cos\left(\frac{2n\pi z}{L}\right),$$

$$V_{II} = \sum_{m,\text{odd}} B_m G_m(r)\cos\left(\frac{m\pi z}{l}\right), \tag{12}$$

where

$$G_m(r) = K_1\left(\frac{m\pi r}{l}\right) I_1\left(\frac{m\pi d}{l}\right) - K_1\left(\frac{m\pi d}{l}\right) I_1\left(\frac{m\pi r}{l}\right). \tag{13}$$

(The exponential fall-off of the field in region II is evident from the asymptotic forms of the modified Bessel functions.) The coefficients in the series expansions for the potentials V_I and V_{II} may be found by applying the appropriate matching conditions at $r = b$. They are

$$V_I(b, z) = V_{II}(b, z), \quad |z| \leq \frac{l}{2};$$

$$V_I(b, z) = 0, \qquad \text{otherwise;} \tag{14a}$$

and

$$-\frac{\partial V_{II}}{\partial r} + \frac{\partial V_I}{\partial r} = \sigma, \quad |z| \leq \frac{l}{2}, \quad r = b. \tag{14b}$$

Integrating Eq. (14a) from $-L/2$ to $L/2$ gives

$$LA_0 = \sum_{m,\text{odd}} B_m J_m{}^0 G_m(b), \tag{15}$$

where

$$J_m{}^n = \int_{-l/2}^{l/2} \cos\left(\frac{2n\pi z}{L}\right) \cos\left(\frac{m\pi z}{l}\right) dz. \tag{16}$$

Multiplying Eq. (14a) by $\cos(2n'\pi z/L)$ and integrating from $-L/2$ to $L/2$ gives

$$\frac{L}{2} A_n I_1\left(\frac{2n\pi b}{L}\right) = \sum_{m,\text{odd}} B_m J_m{}^n G_m(b). \tag{17}$$

Finally, multiplying Eq. (14b) by $\cos(m'\pi z/l)$ and integrating from $-l/2$ to $l/2$ gives

$$-B_m \frac{m\pi}{2} G_m'(b) + \frac{A_0}{b} J_m{}^0 + \sum_n A_n \frac{2n\pi}{L} I_1'\left(\frac{2n\pi b}{L}\right) J_m{}^n = \sigma J_m{}^0. \tag{18}$$

[The primes in Eq. (18) denote differentiation of the Bessel functions with respect to the arguments.] Equations (15) through (18) represent an infinite system of linear equations for the coefficients A_n and B_m. The system may be truncated and the remaining equations solved using standard matrix-inversion routines. For the present problem, only A_0 gives rise to a net force on the beam as it traverses a section of the accelerator (other terms give zero when integrated from $-L/2$ to $L/2$). A modest number of elements in the expansions for V_I and V_{II} are sufficient to determine A_0 to a few-percent accuracy. Some numerical results are presented at the end of this section.

We solve for the gap-induced magnetic field by defining a scalar magnetic potential ϕ and employing a method analogous to that used for the scalar electrostatic potential. (The vector potential A may also be used, but the formulation is somewhat more complicated.) We seek a solution to $\nabla^2\phi = 0$ such that the normal component of B is zero on the conducting boundaries, $\partial\phi/\partial z = 0$ at $z = \pm L/2$, and the tangential components satisfy appropriate matching conditions at $r = b, |z| < l/2$. We write the potential in region I and II as

$$\phi_{\mathrm{I}} = C_0 \frac{r}{b} + \sum_n C_n I_1\left(\frac{2n\pi}{L}\right)\cos\left(\frac{2n\pi z}{L}\right),$$

$$\phi_{\mathrm{II}} = D_0\left(\frac{r}{d} + \frac{d}{r}\right) + \sum_n D_m H_m(r)\cos\left(\frac{2m\pi z}{l}\right), \tag{19}$$

where

$$H_m(r) = I_1\left(\frac{2m\pi r}{l}\right) K_1'\left(\frac{2m\pi d}{l}\right) - I_1'\left(\frac{2m\pi d}{l}\right) K_1\left(\frac{2m\pi r}{l}\right). \tag{20}$$

(For large d, the ρ^{-2} fall-off of B is evident from the first term in the expansion for ϕ_{II}.) In this case, we apply the continuity of B_r and the jump in B_θ at the surface $r = b, |z| < l/2$ to determine the expansion for ϕ_{I} and ϕ_{II}. Specifically,

$$\frac{\partial\phi_{\mathrm{I}}}{\partial r} = \frac{\partial\phi_{\mathrm{II}}}{\partial r}, \quad |z| < \frac{l}{2}, \quad \rho = b;$$

$$\frac{\partial\phi_{\mathrm{I}}}{\partial r} = 0, \quad \frac{L}{2} > |z| > \frac{l}{2}, \quad \rho = b; \tag{21a}$$

and

$$-\frac{1}{r}\frac{\partial\phi_{\mathrm{II}}}{\partial\theta} + \frac{1}{r}\frac{\partial\phi_{\mathrm{I}}}{\partial\theta} = \sigma v, \quad |z| \leqslant \frac{l}{2}, \quad \rho = b. \tag{21b}$$

C_n and D_m may be determined by a procedure analogous to that employed in the electric-field case, and the details are omitted. Again, only C_0 contributes to a net transverse force and a few terms in each series yields reasonable accuracy.

Combining these results, we find that the integrated transverse force experienced by the beam crossing a gap is given by Eq. (5) with

$$l_{\mathrm{eff}} = \frac{1}{2}(\bar{C}_0 - \bar{A}_0), \tag{22}$$

where $\bar{C}_0$ and $\bar{A}_0$ and C_0 and A_0 rescaled by $L/b\sigma$ to have units of length.

In order to check the computational method, calculations were carried out for the geometric parameters treated in Ref. 17; i.e., $L = 30$ cm, $b = 7.5$ cm, $l = 3$ cm and d variable. The results, in Table I, agree well with latest numerical calculations by Neil.[19] Table I also shows that for the magnetostatic force, values of $d \geqslant 4b$ are required before the large-d asymptotic limit is approached. The results displayed in Table I (and Table II) were generated using approximately 200 terms in the series expansions in regions I and II, requiring the inversion of a correspondingly large linear system.

TABLE I

Gap-field coefficients for the parameters $L = 30$ cm, $b = 7.5$ cm, $l = 3$ cm and various values of d

d	15.0	30.0	45.0	60.0	∞
$\bar{A}_0$	0.745	0.745	0.745	0.745	0.745
$\bar{C}_0$	5.91	8.03	8.47	8.62	8.80

TABLE II

Results for RADLAC parameters

d	5.0	10.0	15.0	20.0	∞
$\bar{A}_0$	3.24	3.30	3.30	3.30	3.30
$\bar{C}_0$	6.77	8.74	9.12	9.26	9.40

Subsequent calculations revealed that many fewer terms could be used to achieve reasonably accurate results. Typically, use of about 20 terms was found to yield results within about 5% of those obtained with 200 terms.

In Table II, results for parameters typical of the RADLAC accelerator[4] ($L = 40$ cm, $b = 2.5$ cm, $1 = 4$ cm) are presented. Figure 6 show typical profiles of the electric and magnetic gap fields for the RADLAC parameters. The force is localized roughly to the gap location, decreasing exponentially in the smooth-walled drift tube.

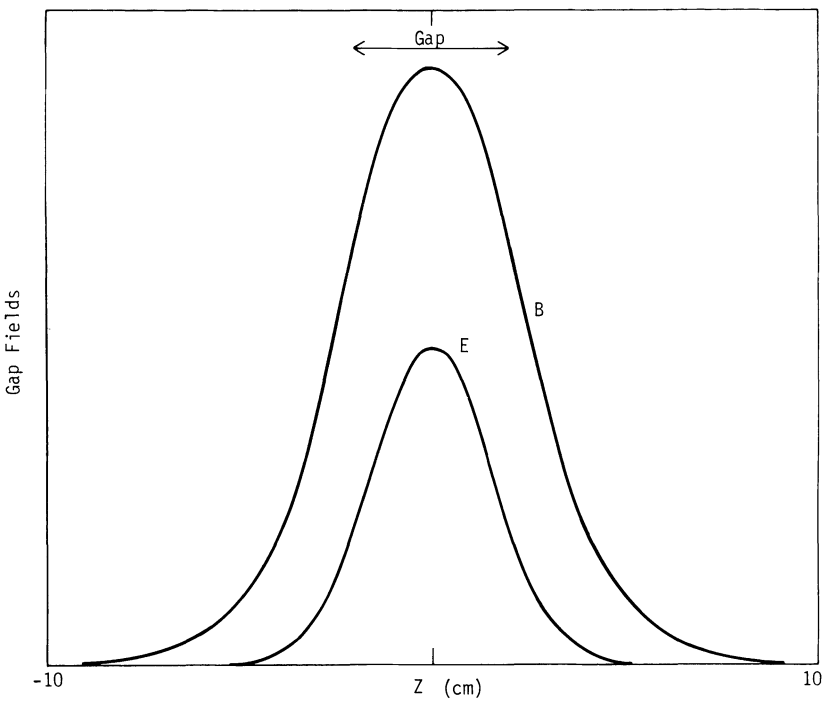

FIGURE 6 Profiles of the $m = 1$ electric (E) and magnetic (M) gap fields for RADLAC parameters. Location of 4 cm gap indicated at top of figure.

IV. EXPERIMENT

The image-displacement effect was investigated experimentally using non-accelerating gaps in a periodic structure, as in Fig. 7. The instability results from the drift-tube gap rather than the accelerating voltage, so the experiment was designed to allow observation of the instability without complications due to acceleration.

Competing gap-induced effects were considered in the design of the experiment. These included the beam-breakup instability[9] and zero-frequency radial oscillations.[4,7,8] Preliminary observations demonstrated that zero-frequency azimuthally symmetric oscillations of the beam (radial oscillations) resulted in beam-current losses in the structure. This is shown in Fig. 8, where up to 30% of the beam current was lost.

The radial oscillations result from the image charge that builds up at the "corner" of each gap. Theory indicates that this effect will fall off rapidly[8] as the gap length is decreased. The radial oscillations were suppressed using thin resistive conductors to cover most of the gap, as depicted in Fig. 9. The two resistive materials used were nylon inserts coated with aerodag and 25 μm stainless-steel foils. Both allowed magnetic

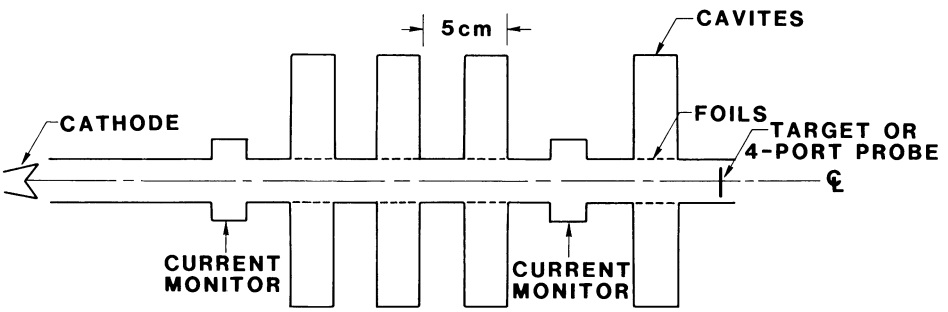

FIGURE 7 Schematic design of image displacement instability experimental apparatus.

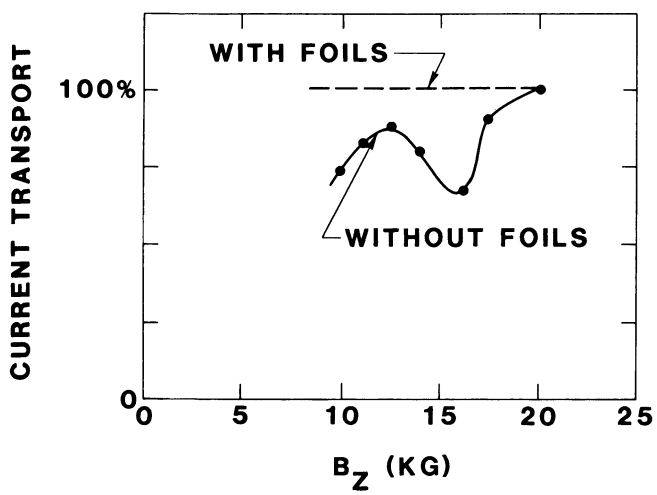

FIGURE 8 Current-transport efficiency with and without foils for experimental series 2.

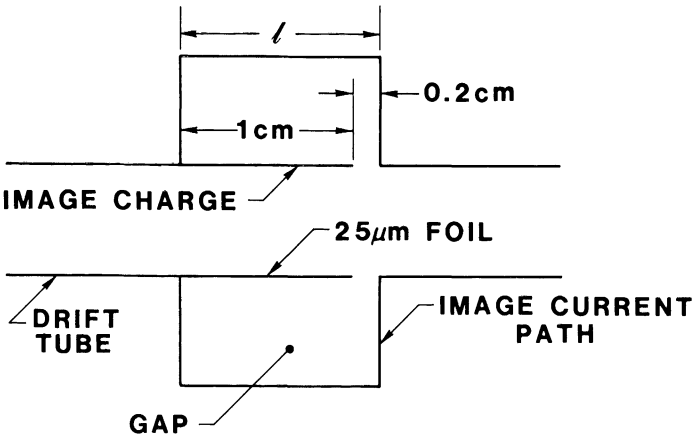

FIGURE 9 Placement of resistive foil to reduce $m = 0$ oscillation amplitude and decouple rf from cavity. Dimensions shown are for experimental series 1.

fields to penetrate in less than a nanosecond while minimizing the displacement of the electric image charge. The result is to minimize radial oscillations by decreasing the electrostatic gap length. (Additionally, the foils increase l_{eff} to approximately l by drastically reducing A_0, strengthening the image-displacement effect). The dashed line in Fig. 8 indicates that the foils were successful in suppressing the radial oscillations. This, incidentally, supports the view that these radial oscillations are purely electrostatic in origin.

The lower limit in achievable magnetic field was dictated by foilless-diode effects. Radial oscillations due to the diode indicated that the minimum operating magnetic field was 8 to 12 kG.

Three sets of experiments were performed to demonstrate both amplitude and phase response of the beam centroid to the drift-tube gaps. Parameters are given in Table III. In each case, the beam was launched straight along the tube axis but slightly off center. Location of the beam at the end of the tube was then measured as a function of axial magnetic field.

Whether the amplitude or phase of the beam displacement is more easily observed is dictated by the diagnostic method used. A witness plate is a target that measures beam-

TABLE III
Experimental Data

	Series 1	Series 2	Series 3
Beam Energy (MeV)	2.9–3.3	2.5–3.0	2.6–3.0
Current (kA)	16–20	24–38	18–24
Radius (cm)	0.75	0.6	0.8
Gap Spacing (cm)	4.9	5.5	6.6
Length (cm)	1.2	2.5	3.2
Number	8	4	4
Magnetic Field (kG)	12–22	6.5–20	11–22
Tube Radius (cm)	1.4	1.4	1.4
Diagnostic method	Probe Array	Witness Plate	Probe Array

induced damage. The time-averaged position of the beam relative to the centroid was measured on these targets. On the other hand, for cyclotron wavelengths comparable to the drift-tube diameter, magnetic probes measure a time-resolved, axially averaged displacement. As a result, the probes are more sensitive to azimuthal drift motion. In terms of the theory developed in a previous section, witness plates are mainly sensitive to $k \simeq k_0$ motion, while the probes detect $k \simeq 0$ motion.

Series 1 was performed in a parameter regime where linear theory predicts minimal growth. The initial offset of the beam was 0.1 cm at an angle $\sim \pi/4$ from the # 1 probe of the position monitor. The initial angle was measured by dividing the slope of the position monitor signal by the slope of the beam current trace. This ratio is proportional to the position (x, y) in each probe monitor plane. Figure 10 displays the dependence of position in the plane on the theoretical drift due to the gaps. The solid line in Fig. 10 corresponds to the theory for $l_{\text{eff}}/l \sim 0.85$, if we include a contribution of about 12% due to drift in the tube between gaps. The observed drift is in reasonable agreement with theory.

Series 2 was diagnosed using witness plates to measure the time-averaged offset approximately one structure period beyond the center of the last gap. The measured displacement is shown as a function of $2\pi/k_0 L$ in Fig. 11. The vertical lines indicate two shots where only a lower bound on displacement could be determined. The two peaks

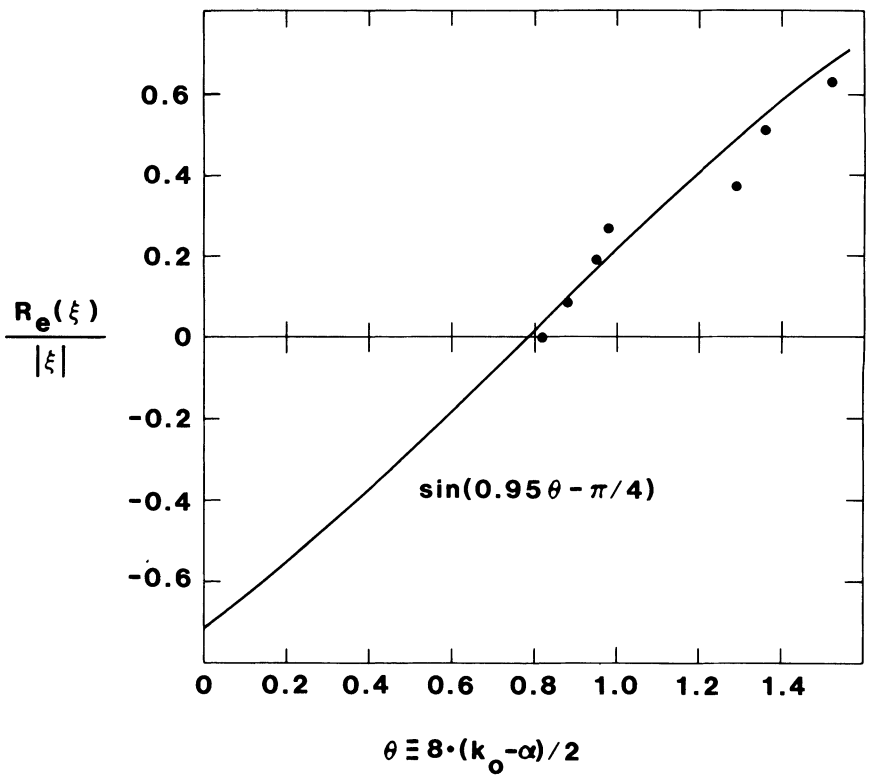

FIGURE 10 Displacement of beam centroid in one transverse direction due to enhanced precession in drift-tube gaps.

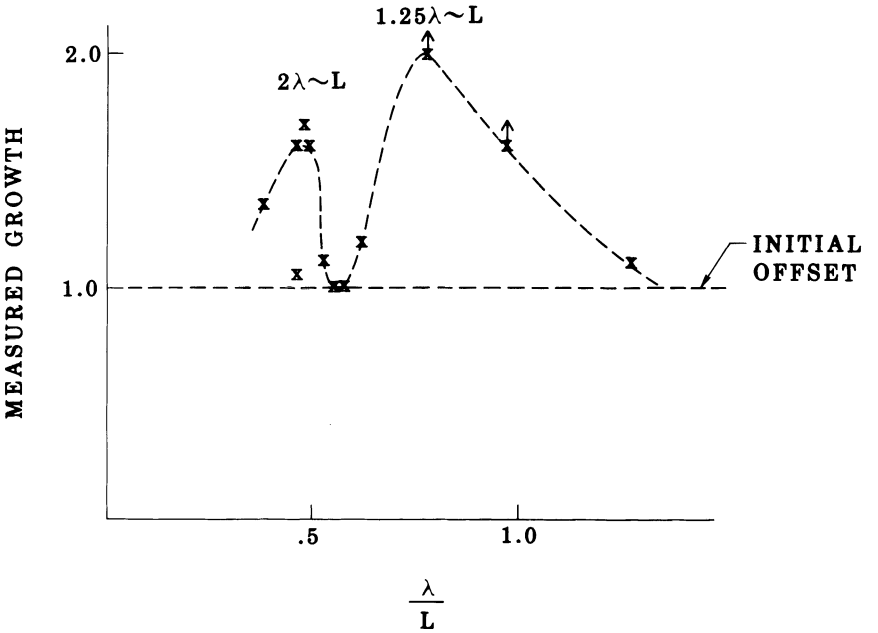

FIGURE 11 Measured growth of beam transverse displacement for experimental series 2. The dashed line is added as an aid to the eye and is not a theoretical curve.

in displacement occur at the expected values of cyclotron wavelength, i.e., where an integral number of cyclotron wavelengths corresponds to the structure period.

We emphasize that the resonant behavior in Fig. 11 is a function of both the instability growth *and* the phase of the cyclotron oscillation. In other words, the resonance could be due to a resonance in the total instability growth (caused by the structure periodicity) or to the exact phase at which an unstable wave is measured.

The simulations discussed in Section V, though run for experimental Series 3, support the latter interpretation. Figure 12 shows computational results equivalent to witness-plate data and displayed in a similar format. In the simulations, the resonant structure is a phase effect. This in turn indicates that the peak displacement of the cyclotron wave occurs approximately at the centre of the last gap.

The third experimental series, which was simulated by the three-dimensional code, was diagnosed using magnetic probes. Drift motion similar to Series 1 was also detected in this run. Simulation results indicated that the maximum growth of the beam displacement was less than a factor of two in the experimental parameter range.

V. COMPUTER SIMULATIONS

Two- and three-dimensional particle-in-cell numerical simulations were performed to assist in interpreting the experimental data of the preceding section and to extend the findings to weaker axial magnetic fields, which were inaccessible experimentally. The simulations were run in cylindrical geometry and emulated conditions of the third experimental series as closely as possible. Figure 13 illustrates boundary conditions. Four non-accelerating gaps, each partially covered by a metallic foil, were located in

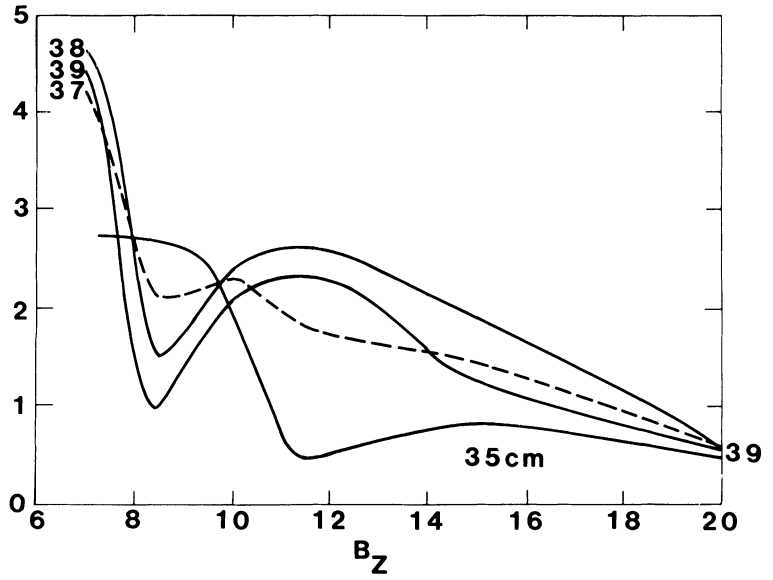

FIGURE 12 Variation of transverse displacement of beam centroid with position from computer simulations of experimental series 3.

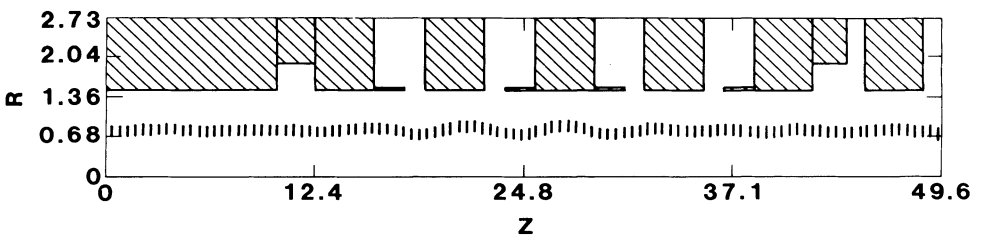

FIGURE 13 Drift-tube geometry and particle locations in z and r for computer simulation of experimental series 3. (B_z = 10 kG.)

the central position of the drift tube. Rogowski-coil sites were located to either side. Wave-transmitting boundary conditions were employed at both ends of the simulation mesh. Nonuniform radial zoning provided enhanced spatial resolution in the beam annulus. Particles were injected at the left with a space-charge-depressed energy of $\gamma = 5.1$ and were absorbed at the right. A 23-kA current was assumed. Examples of position and velocity plots are shown in Figs. 14 and 15.

The two-dimensional simulations were carried out to check the influences of the metal foils. With a guide field of 10 kG but no foils, radial oscillations were so violent that beam current was lost to the walls near the end of the drift tube. Additionally, there was some evidence of bunching instabilities. Foils over the four gaps cut these sausage oscillations to an acceptable level, as shown in Fig. 13. The remaining radial perturbations, due primarily to the shallow Rogowski coil openings, decreased roughly linearly with B_z^{-1}. Although the metal foils shielded the gaps well from electric fields, the beam magnetic fields penetrated easily. The simulations were performed with CCUBE.[20–22]

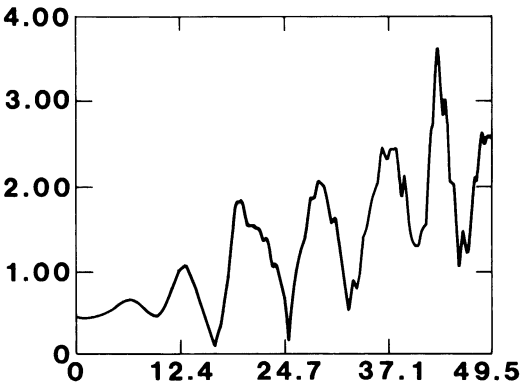

FIGURE 14 Transverse position of beam centroid versus axial location from simulation (B_z = 10 kG.)

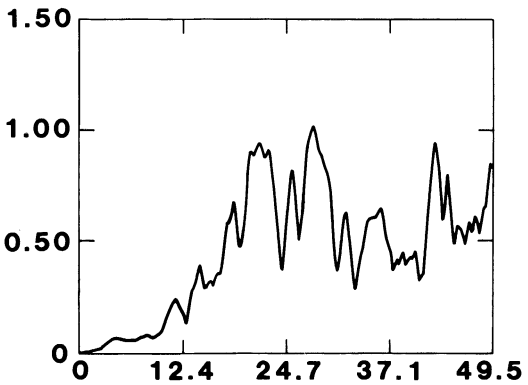

FIGURE 15 Transverse velocity of beam centroid versus axial location from simulation. (B_z = 10 kG.)

The newly developed code IVORY was used to model the image-displacement instability. Conceptually, IVORY is a straightforward extension of CCUBE. Variation of the electromagnetic fields in the third (periodic) spatial coordinate is represented by a sum of Fourier modes. This is not a linearization, although the more nonlinear the physics to be modeled, the more modes are required for an accurate treatment. [For the present study only the $m = 0$ and two $m = 1$ components (sine and cosine) were followed, since nonlinear behavior was not at issue.] Like CCUBE, IVORY has a Galerkin field-particle interface[20,23] and a backward-biased field solver.[24] The code can operate in any orthogonal coordinate system in which at least one coordinate is cyclic. Although IVORY is not yet fully debugged and optimized, its performance was satisfactory for the computations described below.

Seven complete simulations were made, each at a different magnetic-field strength. The annular beam was injected with a rigid displacement of 0.05 cm from the drift tube axis. Figures 14 and 15 depict the typical evolution of the transverse position $|\xi|$ and the transverse velocity $|\dot{\xi}|$ of the beam centroid as a function of axial position. Strong modulation of $|\xi|$ is due both to kicks the beam receives in passing the gap edges and to beating between space-charge and cyclotron components of the transverse oscillations. On the other hand, modulation of $|\dot{\xi}|$ presumably is due only to the gap

forces, since $|\dot{\xi}|$ is dominated by the cyclotron component. It is important to note that the envelopes of $|\xi|$ and $|\dot{\xi}|$ do not grow together, indicating that the mix of space-charge and cyclotron waves is not constant. Moreover, amplification of $|\xi|$ from gap to gap is not uniform. Both observations suggest that large transients are present.

Measured but not displayed here is the oscillation wave number of ξ. Its value for a smoothed-walled tube would be k_0, or 1.15 cm^{-1} for a 10 kg guide field. For the geometry of Fig. 13, the wave number drops to 1.00 cm^{-1}, based on the weighted average of k_0 and $(k_0 + \alpha)/2$ from Eq. (7). The simulation gave 0.95 cm^{-1}, accurate to about 2%.

Peak amplification on $|\xi|$ in traversing the first Rogowski-coil opening and the four gaps is plotted in Fig. 16. Typical uncertainty in measuring the amplification is about 10%. Also shown is the theoretical curve obtained by raising the matrix of Eq. (8) to the fourth power, applying the resulting matrix to the initial-condition vector (a pure space-charge oscillation), and then constructing the absolute length of the out-put vector. This procedure takes account of transients but removes modulation effects associated with the choice of measurement location. (The corresponding asymptotic growth rate appears as the solid curve in Fig. 5.) The effective gap width is set equal to $C_0/2$ in this calculation, because the foils lead to $A_0/2 \simeq 0$. It turns out that l and l_{eff} are comparable. We see from Fig. 16 that the amplification factors as determined from the finite-width gap model and from the simulation are of the same order, but the simulation results exhibit less fine structure as a function of B_z^{-1}. Perhaps the analytical model is failing at low B_z because l/L is not small. In any event, additional research seems desirable.

The range of magnetic fields accessible experimentally also is indicated in Fig. 16. Amplifications from the third set of experiments were less than a factor of two, consistent with theory and simulation.

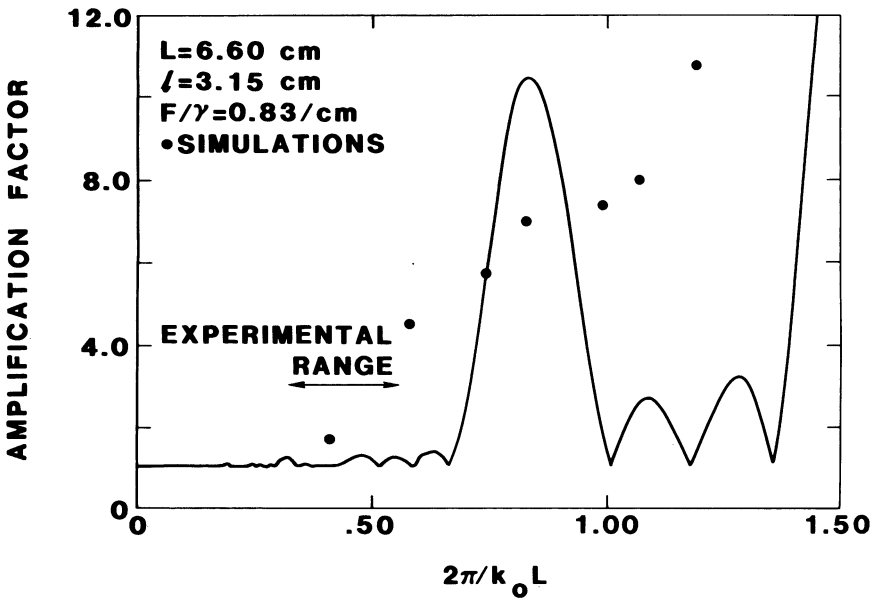

FIGURE 16 Amplification of transverse displacement of beam centroid for experimental series 3 as determined by computer simulation (points) and analytical model (curve).

VI. BEAM-ACCELERATION EFFECTS

Thus far, we have ignored the change in beam energy at each gap in a radial-pulseline accelerator. Within the confines of the models presented in Section II, γ enters only through the phase advance $k_0 L$ between gaps. A systematically changing phase advance can reduce image-displacement instability growth significantly. To examine the influence of γ variation, we have written the simple computer code BALTIC, which integrates Eq. (1) along the accelerator for many beam segments. An impulsive force $F\xi$ of Eq. (5) is applied at gap locations, and γ is changed there as well. Thus, the thin-lens approximation is used, although l_{eff} is sometimes used instead of l in defining F. This approach is conservative in that the thin-lens model overestimates instability growth except at rather weak guide-field strengths. BALTIC is also able to treat beam breakup and $m = 1$ resistive-wall instabilities, either singly or in combination, but such studies are beyond the scope of this paper.

Applying BALTIC to the RADLAC accelerator was gratifyingly uninteresting. Consistent with experimental observations, instability growth was negligible.[25] Consequently, to illustrate the effect of acceleration on image-displacement growth, we chose the parameters of Table IV for study with BALTIC. Ten cases are summarized in Table V.

Case 1 represents the parameters with no acceleration. Overall amplification of transverse oscillations from begining to end of the drift-tube is 7.5, superficially an encouraging result. However, decreasing the guide-field strength by less than a percent in case 2 causes the amplification factor to jump to 1600. Increasing the beam injection energy by the same percentage yields a like result. We are observing here the effect of

TABLE IV

Parameters for Baltic Computations

Injection Current	50 kA
Injection Enengy	2 MeV
Beam Radius	2.0 cm
Beam Thickness	0.2 cm
Drift Tube Radius	2.5 cm
Gap Width	5.0 cm
Gap Voltage	1.0 MV
Gap Separation	100 cm
Guide Field	10 kG

TABLE V

Calculated Image-displacement Instability Growth for Parameters of Table IV

Case	B_z (kG)	l_{eff} (cm)	$\Delta\gamma$	Γ
1	10.0	5.0	0	7.5
2	9.94	5.0	0	1600
3	9.87	5.0	0	340
4	9.51	5.0	0	2.4
5	9.74	5.0	0	2.2
6	10.0	5.0	2.0	470
7	10.23	5.0	2.0	48
8	10.0	1.8	2.0	4.5
9	9.92	1.8	2.0	7.3
10	10.23	1.8	2.0	1.6

sweeping $k_0L/2$ in Fig. 3. Cases 3 to 5 confirm this interpretation. Since shot-to-shot reproducibility of the guide-field strength and beam injection voltage in a real accelerator is uncertain to several percent, the worst-case amplification of initial transverse oscillations by a factor of 1600 or more would occur from time to time.

The effects of acceleration are illustrated by cases 6 and 7. Changing k_0 through γ causes many values of ψ to be sampled by each beam pulse, decreasing the maximum and increasing the minimum possible image displacement instability growth. Additionally, energy transfer between the growing and damped modes at each gap reduces net growth overall. Still, the largest amplification factor of nearly 500 is quite large. Recall, however, that $l = l_{\text{eff}}$ only in the thin-gap limit. A 5-cm wide gap in a 2.5-cm radius drift-tube is not thin. Inserting the value $l_{\text{eff}} = 1.8$ cm into BALTIC drops the peak amplification to 7.3, as indicated in cases 8–10. (Without acceleration, amplification by a factor of 20 or so could occur.) Such low amplification would be acceptable in an operating device, provided good alignment was maintained throughout.

VII. CONCLUSIONS

We have investigated the image-displacement effect analytically, experimentally, and computationally. This work was carried out in the context of radial pulseline accelerators, for which the ratio of gap width to drift-tube radius is not small. Analytically, we extended the usual long-wave length, paraxial-beam model in the simplest possible way to take account of finite-extent gaps by assuming the force exerted on the beam by the gap fields to be applied uniformly over the length of the gap and by more accurately evaluating the average field strengths. The resulting decrease in predicted growth per gap can be substantial.

Four- and eight-gap experiments at high axial magnetic field demonstrated that the analytical formulas are qualitatively correct for both growth rates and precession frequencies. The latter is a useful indicator of the image-displacement effect when amplification is small. Simulations extended the experimental data to weaker guide fields, where some departures from the analytical models became evident. Finally, beam-energy change from gap to gap during acceleration was found to reduce overall instability growth. On the basis of this work, it appears that RADLAC-class accelerators will not be seriously impacted by the image-displacement instability.

The research described here deliberately separated the image-displacement instability from the beam-breakup instability, even though they are, in fact, merely different limits of the same basic phenomenon and tend to occur together. This separation probably is undesirable for more refined studies. We plan to investigate the two more thoroughly in the near future, considering the gaps as lossy cavities appropriate to radial-pulseline accelerators.

ACKNOWLEDGEMENTS

This research was sponsored by the U.S. Air Force Weapons Laboratory, and the experiments were carried out at its electron beam facilities. The computer codes IVORY and CCUBE were developed with support from Los Alamos National Laboratory.

The authors are endebted to R. B. Miller, V. K. Neil, and M. Franz for their advice and assistance. We thank John Leija, Ray Brown and Larry Stevenson for their technical assistance during the course of the experiments.

REFERENCES

1. A. I. Pavlovsky, A. I. Gerasimov, D. I. Zenkov, V. S. Bozamykin, A. P. Klementev, and V. A. Tananakin, *Sov. J. Atom. Ener.* **28**, 432 (1970).
2. A. I. Pavlovsky, V. S. Bozamykin, G. D. Kuleshov, A. I. Gerasimov, V. A. Tananakin, and A. P. Klementev, *Sov. Phys. Dokl.* **20**, 441 (1975).
3. R. B. Miller, K. R. Prestwich, J. W. Poukey, and S. L. Shope, *J. Appl. Phys.* **51**, 3506 (1980).
4. R. B. Miller, K. R. Prestwich, J. W. Poukey, B. G. Epstein, J. R. Freeman, A. W. Sharpe, W. K. Tucker, and S. L. Shope, *J. Appl. Phys.* **52**, 1184 (1981).
5. A. I. Pavlovsky, V. S. Bozamykin, V. A. Savchenko, A. P. Klementev, K. A. Morunov, V. S. Nikolsky, A. I. Gerasimov, V. A. Tananakin, V. F. Basmanov, D. I. Zenkov, V. D. Selemir, and A. S. Fedotkin, *Sov. Phys. Dokl.* **25**, 120 (1980).
6. R. B. Miller, J. W. Poukey, B. G. Epstein, S. L. Shope, T. C. Genoni, M. Franz, B. B. Godfrey, R. J. Adler, and A. Mondelli, IEEE Nuc. Sci. **NS-28**, 3343 (1981).
7. T. C. Genoni, M. R. Franz, B. G. Epstein, R. B. Miller, and J. W. Poukey, *J. Appl. Phys.* **52**, 2646 (1981).
8. R. J. Adler, AMRC-R-300 (Mission Research Corporation, Albuquerque, 1982).
9. R. J. Adler, T. C. Genoni, and R. B. Miller, IEEE Nuc. Sci. **NS-28**, 3467 (1981).
10. B. B. Godfrey, R. J. Adler, M. M. Campbell, D. J. Sullivan, and T. C. Genoni, *Proc. 1981 Linear Accelerator Conference* (Santa Fe), to be published.
11. J. W. Poukey and J. R. Freeman, *Proc. 1981 Linear Accelerator Conference* (Santa Fe), to be published.
12. B. B. Godfrey and B. G. Epstein, AMRC-N-142 (Mission Research Corporation, Albuquerque, 1980).
13. B. G. Epstein and J. W. Poukey, *Phys. Fluids* **23**, 1956 (1980).
14. B. B. Godfrey, AMRC-R-345 (Mission Research Corporation, Albuquerque, 1982).
15. T. C. Genoni, unpublished.
16. C. H. Woods, *Rev. Sci. Instr.* **41**, 959 (1970).
17. V. K. Neil, UCID-17838, (Lawrence Livermore National Laboratory, 1978).
18. V. K. Neil, UCID-17976, (Lawrence Livermore National Laboratory, 1978).
19. V. K. Neil, private communication.
20. B. B. Godfrey, LA-7687-MS (Los Alamos National Laboratory, 1974).
21. L. E. Thode, B. B. Godfrey, and W. R. Shanahan, *Phys. Fluids* **22**, 747 (1979).
22. M. M. Campbell, D. J. Sullivan, and B. B. Godfrey, AMRC-R-341 (Mission Research Corporation, Albuquerque, 1982).
23. B. B. Godfrey and L. E. Thode, *Proc. Seventh Conf. Numerical Simulation of Plasmas* (New York University, 1975), p. 87.
24. B. B. Godfrey, *Proc. Ninth Conf. Numerical Simulation of Plasmas* (Northwestern University, 1980), paper OD-4.
25. R. B. Miller and R. J. Adler, unpublished.